Optical Engineering

OpticalEngineering.SPIEDigitalLibrary.org

Focusing with planar microlenses made of two-dimensionally varying high contrast gratings

Annett B. Klemm
Daan Stellinga
Emiliano R. Martins
Liam Lewis
Liam O'Faolain
Thomas F. Krauss

SPIE.

Focusing with planar microlenses made of two-dimensionally varying high contrast gratings

Annett B. Klemm,[a,*,†] Daan Stellinga,[a,†] Emiliano R. Martins,[b] Liam Lewis,[c] Liam O'Faolain,[d] and Thomas F. Krauss[a,d]
[a]University of York, Photonics Group, Department of Physics, Heslington, York YO10 5DD, United Kingdom
[b]Universidade Federal de São Carlos, Departamento de Fisica, São Carlos, São Paulo 13565-905, Brazil
[c]Tyndall National Institute, Photonic Device Dynamics Group, Lee Maltings, Cork, Ireland
[d]University of St. Andrews, School of Physics & Astronomy, North Haugh, St Andrews KY16 9SS, United Kingdom

Abstract. We report on the focusing performance of reflective two-dimensionally varying high contrast grating lenses based on silicon. The combination of their subwavelength nature and their high refractive index contrast makes it possible to create highly tolerant and planar microlenses. We used a rigorous mathematical code to design the lenses and verified their performance with finite element simulations. We also investigated the effects of grating thickness, angle, and wavelength of incidence in these simulations. Experimentally, we show the evolution of the beam profile along the optical axis for a lens with a high (0.37) numerical aperture. We have explored a wide range of numerical apertures (0.1–0.93) and show that the lenses behave as expected across the full range. Our analyses demonstrate the large design flexibility with which these lenses can be made along with ease of fabrication and potential for a number of applications in micro-optics. [DOI: 10.1117/1.OE.53.9.095104]

Keywords: diffractive optics; microlens; flat optics; photonic crystals; high index contrast; numerical aperture.

Paper 140555P received Apr. 2, 2014; revised manuscript received Aug. 7, 2014; accepted for publication Aug. 18, 2014; published online Sep. 11, 2014.

1 Introduction

The phenomenon of guided-mode resonances[1] is of major interest in micro-optics as a basis for designing optical devices on a very small footprint, such as spectrally narrow bandpass or notch filters,[2] mirrors reflecting light over a large wavelength range,[3] angle-tolerant and polarization-independent mirrors,[4,5] flat focusing reflectors,[6,7] or microelectromechanical systems (MEMS) scanners.[8] The common features of all these devices are the subwavelength scale and the high refractive index contrast of their grating dimensions, which for normal incidence and suitable design of the parameters such as film thickness, period, and fill factor result in diffraction into a single order, with all other orders becoming evanescent, eventually leading to almost 100% reflection or transmission. Controlling the reflected phase is achieved via the grating period and/or fill factor and is essential for creating functional elements such as lenses, which have been demonstrated numerically[7,9] and experimentally.[6,10] We have previously demonstrated[10] a silicon high contrast grating (HCG) lens with a numerical aperture (NA) of 0.37 and a spot size close to the diffraction limit, which was achieved by incorporating several 2π phase jumps. Here, we examine these lenses in more detail to study their wavelength dependence and their off-axis performance, and to demonstrate the focusing operation over a wide range of parameters.

2 Lens Design

We use a layer of amorphous silicon deposited by electron beam evaporation on a glass substrate as the high index material. Throughout the paper, we consider near-infrared light at 980 or 1064 nm that is incident with transverse–magnetic (TM) polarization, i.e., with the magnetic field vector parallel to the grating ridges. Devices are designed to operate in reflection and we use the rigorous coupled wave analysis[11] (RCWA) method for the numerical simulation. In all following simulations, we included the dispersion and absorption values of amorphous silicon derived from ellipsometry measurements performed by our collaborators (see Acknowledgments). The RCWA allows us to calculate a reflectivity and phase map as a function of the grating period and fill factor for a given thickness of silicon (see Fig. 2). A path-finding algorithm[12] then extracts all values of period and duty cycle from the phase maps that are required to obtain a quasicontinuous phase response between 0 and 2π and in order to implement the parabolic phase profile required for constructing a lens. At the same time, the routine checks for the highest possible reflectivity value. We note that it is not always possible to achieve high reflectivity (>95% without inclusion of absorption) across the full phase range, which leads to some undesired transmission as shown in Fig. 1. Besides the calculated phase paths, a low but non-negligible absorption of the amorphous silicon in the considered wavelength range contributes to an overall decrease in reflectivity to about 80% at the utilized thickness of about 300 nm (Fig. 2).

As we are interested in microlenses with tight focusing characteristics and high numerical apertures, multiple phase changes with several 2π jumps are required. The result (see Fig. 1) resembles a Fresnel lens consisting of several concentric rings for which the phase values are identical; in contrast to the Fresnel lens, however, the phase is correct at any point in the plane, which leads to a much higher

*Address all correspondence to: Annett B. Klemm, E-mail: annett.klemm@york.ac.uk

†These authors contributed equally to the manuscript.

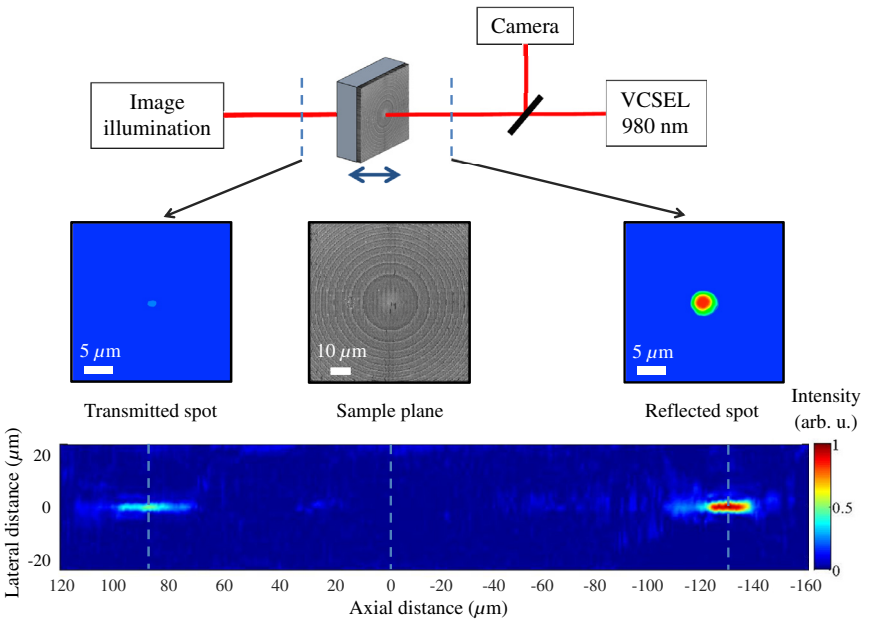

Fig. 1 Optical setup and measured beam profiles for an HCG lens with NA = 0.37, focal length of 100 μm, and optimized for normally incident TM-polarized radiation at 980 nm. Top: Schematic of the optical setup. Middle: Imaging planes of the reflected spot (right) and the transmitted spot (left), with the sample shown as SEM image (center). Bottom: Montage of slices taken along the optical axis showing normalized intensity as a function of both lateral and axial distances for the described HCG lens.

efficiency, i.e., we estimate that 70%–80% of the incoming intensity is concentrated in the focal spot. This efficiency estimation is based on the power flow through the focal region in a typical FEM simulation. Further details of the design routine can be found in Ref. 10. Following simple geometrical rules, we define the numerical aperture of our HCG lens via its entrance pupil or diameter D, focal length f, and surrounding medium n as:

$$\mathrm{NA} = n \cdot \sin\left[\tan^{-1}\left(\frac{D}{2f}\right)\right]. \tag{1}$$

We fabricated the HCG lenses using standard silicon processing technologies involving the patterning of an electron sensitive resist with electron beam lithography, transferring the pattern into the amorphous silicon via reactive ion-beam etching and finally stripping off the remaining resist.

3 Lens Performance

3.1 *Beam Profile*

We analyzed the beam profile of a fabricated HCG lens—optimized for TM polarization, normal incidence at

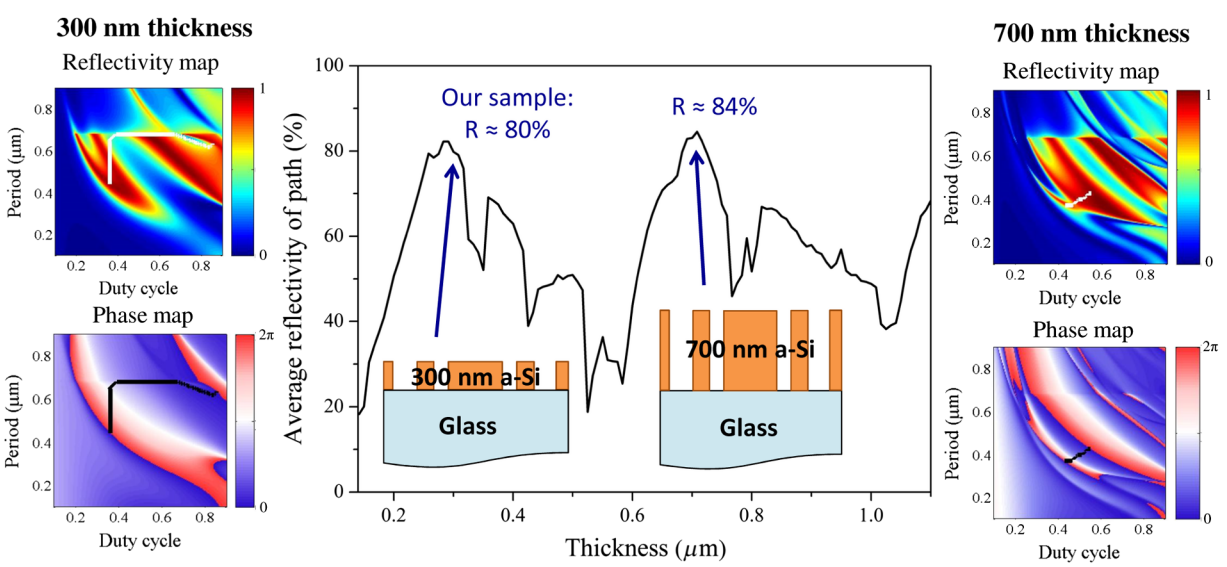

Fig. 2 Simulated average reflectivity of the optimal identified path as a function of the grating thickness with two thickness examples given. Highlighted next to the graph are the maps of reflectivity and phase as a function of the grating parameters period and duty cycle, together with the path (in white and black) for our utilized thickness of 300 nm (left) and an exemplified thicker one at 700 nm (right).

980 nm, and reflection along the optical axis—by illuminating the sample with a TM-polarized and collimated 980-nm vertical-cavity surface-emitting laser (VCSEL) beam using a beamsplitter, while imaging with a complementary metal-oxide-semiconductor camera along the optical axis of the system (Fig. 1). The result is shown in Fig. 1 for a lens with a diameter of 80 μm, a target focal length of 100 μm, and a numerical aperture of 0.37, together with a scanning electron micrograph (SEM) of the lens itself.

Light incident from the right is reflected at the sample and produces a focal spot at a focal length of $f \approx 130$ μm. Due to the double focusing property of these HCG lenses,[7] a spot at the rear focal plane of the HCG lens simultaneously appeared at a distance of about 90 μm with similar axial dimensions. As the transmitted spot occurs inside the glass substrate, its focal length is shorter than that of the reflected spot. For the reflected spot, we observe an axial resolution d (taken where intensity drops to 1/e) of approximately 15 μm, which is close to the expected value of $\approx$10 μm [from $d = \lambda/(\mathrm{NA})^2$]. The lateral spot sizes s of approximately 5 μm are also close to the expected diameter of an Airy disk as derived from diffraction theory ($s = 1.22\lambda/\mathrm{NA} = 3.2$ μm), an agreement that highlights the high performance of these lenses. Further details on the lateral spot size, on the assessment of the quality of the fabricated lens by means of scanning electron micrographs as well as on a study of the polarization dependence can be found in our previous paper.[10]

3.2 *Influence of High-Index Layer Thickness*

The performance of an HCG depends both on the grating parameters and the thickness of the high index layer as it is determined by an interplay between the Fabry–Pérot (F–P) resonances of the slab and the Bragg resonances of the grating.[13] In this section, we are not concentrating on a specific lens structure, but we are aiming to highlight the effect of different layer thicknesses on the attainable average reflectivity for a path following a parabolic phase profile. In this way, we are able to provide a measure for the best possible design at relevant thickness values. In order to assess the dependence of reflectivity on layer thickness for an arbitrary HCG lens design, we calculated the reflectivity for layer thicknesses between 140 nm and 1.1 μm for a normally incident plane wave at a wavelength of 980 nm using RCWA and the abovementioned path-finding algorithm (Fig. 2). The reflectivity was not simply taken at the maximum point, but averaged over all phase values between 0 and 2π, thereby representing the average reflectivity of a grating lens.

We note that certain thickness values, in particular around 300, 700 nm, and beyond, exhibit average reflectivities of 80% and above, whereas several dips are visible below 200, around 600, and 1000 nm. The minimum below 200 nm comes from the fact that the different mode types within the grating are too far apart in parameter space to provide sufficiently high reflectivity. On the other hand, the other dips beyond this area are related to minima in the F–P resonances of the slab. As we are aiming for an effective reflective lens, we highlighted in the figure the two thicknesses of 300 and 700 nm at which the highest average reflectivities are achieved. As thicker grating layers are more difficult to etch in practice and will be ultimately limited by absorption, we opted for gratings with a thickness of approximately 300 nm in our experiments. Also, by comparison of the path characteristics of thinner (300 nm) and thicker (700 nm) layers with high average reflectivity (Fig. 2, left and right of the main graph), it becomes clear that the calculated paths are shorter for gratings with larger thicknesses. This is due to the fact that for increasing layer thicknesses more guided-mode resonances are contributing to the grating response, hence shorter phase paths are available, which significantly decrease the fabrication tolerance.

3.3 *Wavelength Dependence*

The wavelength dependence of the grating lenses was studied using simulations in COMSOL Multiphysics, which is based on the finite element method. We used a one-dimensional grating lens designed for an incident plane wave at a wavelength of 980 nm and simulated its response for illumination with a range of different wavelengths between 830 and 1130 nm (Fig. 3).

The simulated grating had a finite lateral extent and was infinite along the plane of the ridges. The calculated time-averaged power flow was normalized with respect to the incident power on the grating. The specific grating studied here was designed for normal incidence, TM-polarized light, and consisted of a 330-nm thick layer of amorphous silicon on glass with a focal length of 60 μm and an NA of 0.64. The behavior shown is typical for HCG lenses, as we have verified with similar designs.

We note that the focusing property is maintained over a broad range of wavelengths, although the intensity in the focal spots drops off to about a quarter at the lowest wavelength (830 nm) and half at the highest wavelength (1130 nm) used in the experiment. As shown in Figs. 3(b) and 3(d), the lateral confinement of the focal spots is maintained even at the extreme wavelengths, although the spots are further extended in the axial direction. These good focusing properties only depend on the relative phase profile, which is largely maintained across the wavelength range studied here.

The reflectivity of the resonances changes more unpredictably, which is due to the fine balance between phase and reflection in the path-finding algorithm referred to earlier. The variation in focal length with wavelength apparent from Fig. 3(a) is due to a change in optical path lengths in air. Focusing occurs at the point where all the rays from the grating arrive with the same phase, and since the physical distance over which the phase changes depends on the wavelength, so does the focal distance. More specifically, if we take the original phase profile equation Eq. (2) of the grating lenses with ϕ being the target phase, r the distance from the center of the lens, f the focal length, and λ the operating wavelength,

$$\phi = \frac{2\pi}{\lambda}\left(\sqrt{r^2 + f^2} - f\right) \tag{2}$$

and rewrite it to

$$f = \frac{\pi \cdot r^2}{\lambda \cdot \phi} - \frac{\lambda \cdot \phi}{4\pi}, \tag{3}$$

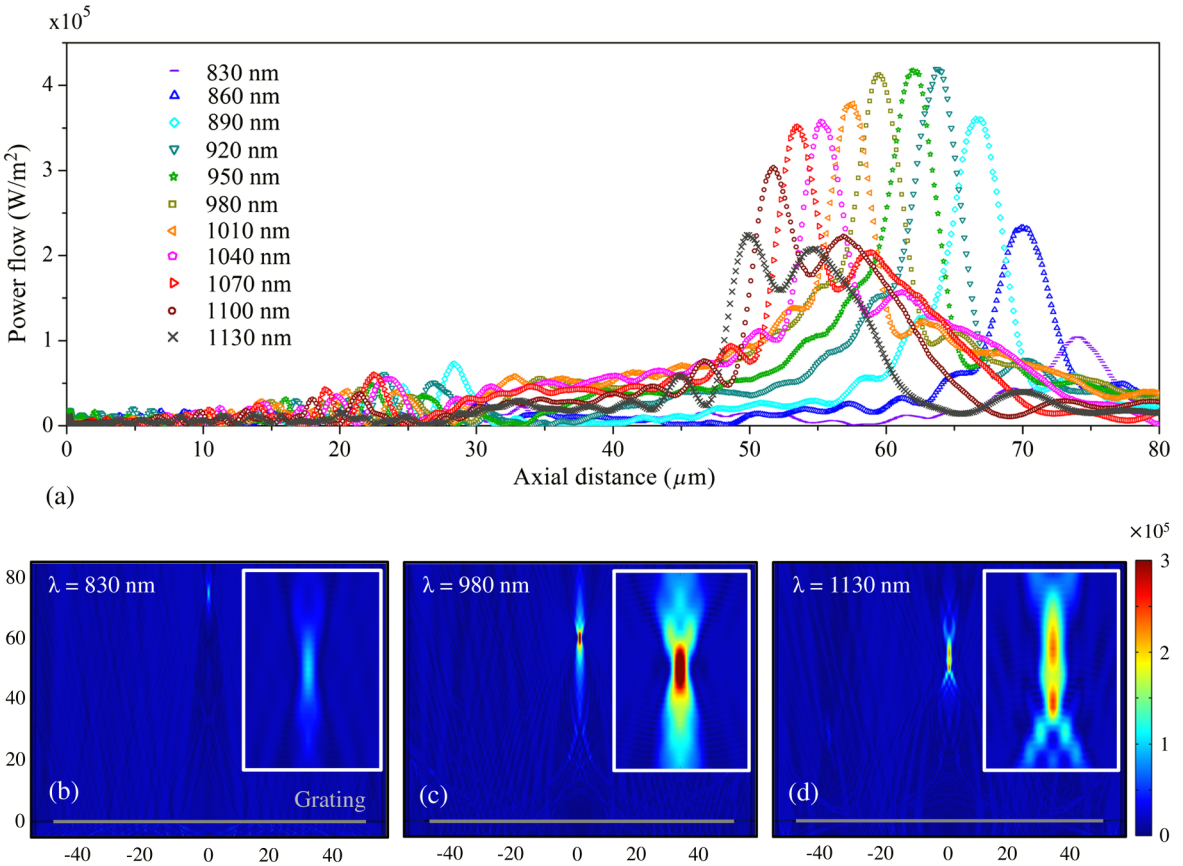

Fig. 3 Wavelength dependence of an HCG lens of $f = 60$ μm and NA $= 0.64$: (a) Time-averaged power flow along the optical axis for different wavelengths of incidence. Field plots of the power flow with respect to the lateral (x-axis) and axial distances (y-axis), given in microns, for a wavelength of incidence of (b) 830 nm, (c) 980 nm, and (d) 1130 nm. Insets illustrate a close-up view of the focal spot region. The colorbar shows the time-averaged power flow in W/m^2.

then for $r \gg \lambda$ ϕ, the focal length f scales as λ^{-1}, which agrees with our results.

3.4 *Angle of Incidence*

A similar lens design was used for a simulation study of the angular dependence, again with the finite element method. We kept the wavelength constant at 980 nm and changed the angle of incidence θ from 0 to 12 deg (Fig. 4).

For normal incidence, the power flow into the focal spot is maximal and a relatively large focus of about 15 μm is observed along the optical axis. The lenses can tolerate a few degrees of deviation, but then quickly lose their properties for angles above 8 deg, with the focal spot reaching the noise level for a 12 deg input angle. The location of the focal spot follows the input axis, as expected. Overall, we note that grating lenses are much more sensitive to input angle than classical refractive lenses.

A comparison with the results from the wavelength dependence proves to be instructive: For periodic resonant structures with period Λ, a change of incidence angle usually corresponds to a change in wavelength because of the equation:

$$|\vec{k}| = |\vec{k}_{//} + m \cdot \vec{G}|, \tag{4}$$

in which $\vec{k}$ is the wave vector of the incident light, $\vec{k}_{//}$ the component of the incident wave vector in the plane of the grating, m is an integer, and $\vec{G}$ is the grating vector, which corresponds to $2\pi/\Lambda$. Substituting the wavelength and angular dependence into Eq. (4), it becomes:

$$\frac{2\pi}{\lambda} = \sin(\theta) \cdot \frac{2\pi}{\lambda} + m \cdot \frac{2\pi}{\Lambda} \tag{5}$$

or

$$\frac{2\pi}{\lambda_{\text{eff}}} = |m \cdot \vec{G}|, \tag{6}$$

where

$$\lambda_{\text{eff}} = \frac{\lambda}{1 - \sin(\theta)}. \tag{7}$$

We would, therefore, expect a change of angle to affect our grating lenses in much the same way as an increase in wavelength. Comparing Figs. 3 and 4, and using Eq. (7), we find that this line of reasoning holds fairly well in terms of the intensity of the focal spot. For example, an incidence angle of 6 deg corresponds to a wavelength of 1094 nm, at which point we would expect the intensity to have decreased by about 25% in the wavelength plot, as it does in the angular plot.

As the shift of the focal spots in Fig. 3 originates from optical path length differences after the grating, we would

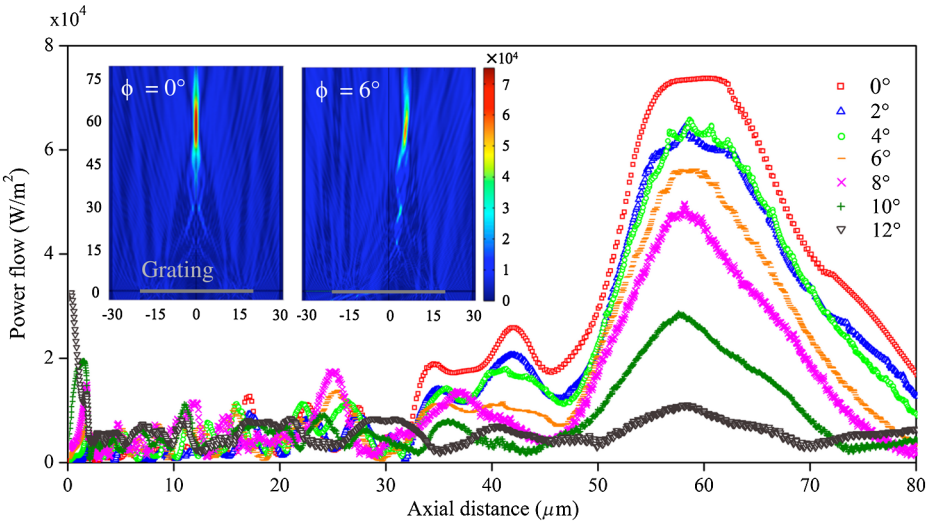

Fig. 4 Influence of angle of incidence θ for an HCG lens with $D = 40$ μm and $f = 60$ μm on the power flow along the optical axis. The two insets show the power flow in W/m^2 upon the grating as a function of the axial (x-axis) and lateral distances (y-axis), given in microns, for normal incidence and incidence angle of 6 deg.

not expect a similar shift of the focal spot position with angle, which is indeed what we observe.

We need to stress that this is only an example grating structure. For different design wavelengths, thicknesses, polarizations, or materials, different wavelength and angle dependencies will apply. An indication of the spectral bandwidth can be gleaned from the RCWA map and phase path for a grating (see Fig. 2) as a change in wavelength, and therefore, the angle roughly corresponds to a change in period, and a shift of the path up or down along that axis on the RCWA maps. The more the path can be shifted along the y-axis (period) without significantly changing the phase and reflectivity response, the less dependent the resulting lens will be on the wavelength and the angle.

Due to the similarity of the grating-based lens and a blazed diffractive system,[14] achromatic effects such as the intensity drop in the focal spot for incident wavelengths or angles different from the design could be partially explained by the physics of blazed gratings; however, an in-depth comparison of the two systems is beyond the scope of this paper and might be subject of a future investigation.

3.5 *Scan of Different Numerical Apertures*

It is instructive to further explore the parameter range available with these lenses, also in view of possible applications such as in the field of biology in which a common wavelength is 1064 nm (due to low absorption coefficient). To this end, we designed, fabricated, and characterized a large number of reflective HCG lenses with different diameters and focal lengths which were optimized for a TM-polarized input at 1064 nm. The optical setup used was the same as shown in Fig. 1 apart from the replacement of the 980-nm VCSEL with the 1064-nm laser. Again, the laser beam was TM polarized, collimated, and normally incident on the sample. The numerical apertures varied between 0.1 and 0.93, as shown in Fig. 5.

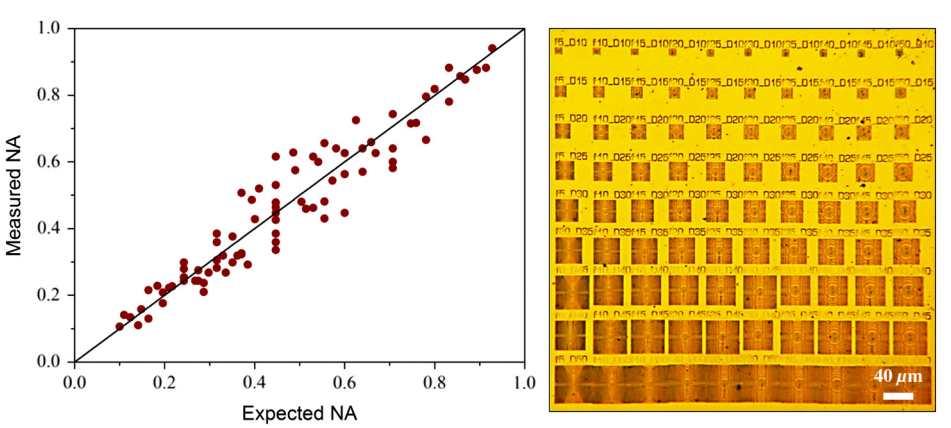

Fig. 5 (a) Comparison of expected and measured numerical apertures, (b) optical image of fabricated HCG lenses with different numerical apertures.

We recorded the focal distance for each lens and compared it to the design value; Fig. 5 shows that a good agreement between design and experiment is achieved across the full range of numerical apertures; in fact, the good agreement at higher numerical apertures is testimony to the high quality of our fabrication technology.

4 Conclusion

We have presented compact and planar silicon microlenses based on two-dimensionally varying HCGs, and have provided detailed information about their performance. We have discussed the influence of the grating thickness and the dependence on the angle and wavelength of incidence. We note that these lenses, once an optimal thickness has been identified, perform very well over a broad spectral range and allow for small angular fluctuations. Moreover, we have experimentally assessed the beam profile and show focusing both in reflection and in transmission. In addition, HCG lenses covering a large range of numerical apertures have been fabricated and characterized, highlighting the wide range of parameters available with these lenses. Due to the high index contrast and planarity, HCG lenses are very suitable for applications in microfluidics, as their performance will not deteriorate in an aqueous environment, unlike conventional microlenses based on polymers[15] or glass.[16] The feasibility of producing arrays of HCG microlenses is also straightforward. Another promising application is the collimation of micron-sized light sources, thereby replacing bulky beam shaping elements.

Acknowledgments

This manuscript refers to a prior proceedings paper.[17] Our sincere thanks go to Professor Kishan Dholakia, University of St. Andrews, for providing us with the 1064-nm fiber laser used in Fig. 5. We thank our collaborators at the University of Pavia, Italy, for the spectroscopic ellipsometry measurements of the utilized amorphous silicon. We kindly thank the European Union for the financial support through Marie Curie Action FP7-PEOPLE-2010-ITN Project No. 264687 "PROPHET".

References

1. S. S. Wang and R. Magnusson, "Theory and applications of guided-mode resonance filters," *Appl. Opt.* **32**(14), 2606–2613 (1993).
2. S. Tibuleac and R. Magnusson, "Reflection and transmission guided-mode resonance filters," *J. Opt. Soc. Am. A* **14**(7), 1617–1626 (1997).
3. C. F. R. Mateus et al., "Ultrabroadband mirror using low-index cladded subwavelength grating," *IEEE Phot. Techn. Lett.* **16**(2), 518–520 (2004).
4. S. Kroker et al., "Enhanced angular tolerance of resonant waveguide grating reflectors," *Opt. Lett.* **36**(4), 537–539 (2011).
5. D. Zhao et al., "Polarization independent broadband reflectors based on cross-stacked gratings," *Opt. Express* **19**(10), 9050–9055 (2011).
6. D. Fattal et al., "Flat dielectric grating reflectors with focusing abilities," *Nat. Photonics* **4**(7), 466–470 (2010).
7. F. Lu et al., "Planar high-numerical-aperture low-loss focusing reflectors and lenses using subwavelength high contrast gratings," *Opt. Express* **18**(12), 12606–12614 (2010).
8. I. W. Jung, S. Kim, and O. Solgaard, "High-reflectivity broadband photonic crystal mirror MEMS scanner with low dependence on incident angle and polarization," *J. Microelectromech. Syst.* **18**(4), 924–932 (2009).
9. Y. Wang et al., "Design method to enhance the transmittance of a structured lens based on nonperiodic sampling," *Opt. Eng.* **50**(1), 018001 (2011).
10. A. B. Klemm et al., "Experimental high numerical aperture focusing with high contrast gratings," *Opt. Lett.* **38**(17), 3410–3413 (2013).
11. M. G. Moharam and T. K. Gaylord, "Rigorous coupled-wave analysis of planar-grating diffraction," *J. Opt. Soc. Am.* **71**(7), 811–818 (1981).
12. E. W. Dijkstra, "A note on two problems in connexion with graphs," *Numer. Math.* **1**(1), 269–271 (1959).
13. S. Fan and J. D. Joannopoulos, "Analysis of guided resonances in photonic crystal slabs," *Phys. Rev. B* **65**(23), 235112 (2002).
14. P. Lalanne, "Waveguiding in blazed-binary diffractive elements," *J. Opt. Soc. Am. A* **16**(10), 2517–2520 (1999).
15. J. Chen et al., "Variable-focusing microlens with microfluidic chip," *J. Micromech. Microeng.* **14**(5), 675 (2004).
16. C. H. Lin et al., "Fabrication of microlens arrays in photosensitive glass by femtosecond laser direct writing," *Appl. Phys. A* **97**(4), 751–757 (2009).
17. A. B. Klemm et al., "Characterization of planar microlenses made of high contrast gratings," *Proc. SPIE* **8995**, 89950L (2014).

Annett B. Klemm received her degree in biomedical engineering from the University of Applied Sciences Jena, Germany, and her MSc degree in photonics from both KTH, Stockholm, Sweden, and the University of St. Andrews, Scotland. In 2011, she commenced her PhD at the Microphotonics and Photonic Crystals Group at the University of St. Andrews, and continued after the group's relocation to the University of York, England. Her work focuses on microfabrication processing of diffractive metastructures and tunable filters.

Daan Stellinga received his BSc degree in physics in 2010 from Leiden University, located in the Netherlands, and obtained his MSc degree in experimental physics in 2012 at the same university. During this time he completed an internship at the FOM Institute AMOLF in Amsterdam. Currently, he is pursuing a PhD in physics at the University of York. His research interests are predominantly in the area of light–matter interaction in photonic structures.

Emiliano R. Martins graduated in electrical engineering from the University of Sao Paulo in 2005. He obtained his master's degree in electrical engineering from the University of Sao Paulo in 2008 and a master's degree in photonics from the European Master of Science in Photonics in 2010. He completed his PhD degree in physics from the University of St. Andrews in 2014.

Liam Lewis received his PhD degree from the Tyndall Institute in Cork in 2007, examining the critical aspect of contact formation to GaN-based light-emitting diodes. After a one-year post doc, he moved to Cork Institute of Technology to take up a position as a researcher in the Centre for Advanced Photonics and Process analysis (CAPPA). He now heads up the center dealing with all aspects of the photonic research conducted at the center.

Liam O'Faolain is a lecturer at the School of Physics and Astronomy at the University of St. Andrews. He is one of the leading authorities on disorder and loss in photonic crystals, and has designed and realized the world's best slowlight waveguides to date. One of his group's main research goals is the realization of a new family of low-power optical interconnects based on photonic crystal cavities.

Thomas F. Krauss leads the photonics group at the University of York. The aim of his research is to understand and control the light–matter interaction in photonic nanostructures, and to build functional devices that make use of this understanding. His activity spans the study of fundamental concepts such as nonlinearity and enhanced light emission to more applied areas such as nanolasers, optical switches and, more recently, biosensors and solar cells.